This is a preprint, the final version is subject to change, of the American Mineralogist (MSA)
Cite as Authors (Year) Title. American Mineralogist, in press.
(DOI will not work until issue is live.) DOI: http://dx.doi.org/10.2138/am-2017-6125

REVISION 1

Physicochemical controls on bismuth mineralization, Moutoulas, Serifos Island, Cyclades, Greece

MICHALIS FITROS[1], STYLIANOS F. TOMBROS[1], ANTHONY E. WILLIAMS-JONES[2], BASILIOS TSIKOURAS[1,3], ELENI KOUTSOPOULOU[1], KONSTANTIN HATZIPANAGIOTOU[1]

[1]Department of Geology, Section of Earth Materials, University of Patras, Rion, 26500, Patras, Greece

[2]Department of Earth and Planetary Sciences, 3450 University Street, Montreal, Quebec H3A 2A7, Canada

[3]Universiti Brunei Darussalam, Faculty of Science, Physical and Geological Sciences, Jalan Tungku Link, BE1410 Gadong, Bandar Seri Begawan, Brunei Darussalam

Abstract: The 11.6 to 9.5 Ma Serifos pluton intruded schists and marbles of the Cycladic Blueschist unit, causing thermal metamorphism, the development of magnetite Ca-exo- and endo-skarns and the formation of low-temperature vein and carbonate-replacement ores. Potentially, the most important ores occur in the Moutoulas prospect where the mineralization in retrograde skarn and quartz veins culminated with the deposition of native bismuth. A combination of fluid inclusion microthermometry and isotope geothermometry suggests that the Moutoulas mineralization formed at a hydrostatic pressure of ~ 100 bars, from moderate-to-low temperature (~190°-250°C), and low-salinity (1.3-5.6 wt. % NaCl equivalent) fluids. The calculated $\delta^{34}S_{H2S}$ compositions are consistent with the ore fluids having been derived from the Serifos pluton. Bismuth mineralization is interpreted to have occurred as a result of wall-rock interaction and mixing of a Bi-bearing ore fluid with meteoric waters. Native bismuth and bismuthinite deposited at ~ 200°C, near neutral pH

Always consult and cite the final, published document. See http:/www.minsocam.org or GeoscienceWorld

(6.5), low fS_2 (< -16.5), and low fO_2 (< -44). Supergene alteration in Serifos led to the oxidation of native bismuth to bismite and bismutite.

Keywords: Native bismuth, retrograde skarn, supergene alteration, Moutoulas, Serifos.

Introduction

Knowledge of the aqueous geochemistry of bismuth, in particular, the physicochemical controls of its transportation and deposition is still incomplete. Experimental and theoretical studies (e.g., Skirrow and Walshe 2002; Tooth et al. 2008; Mavrogenes et al. 2010; Henley et al. 2012; Etschmann et al. 2016) suggest that Bi can be mobile either in vapors at high temperature or in the liquid as complexes of Bi^{3+} ions with hydroxyl and chloride ions, e.g., $Bi_n(OH)_m^{+x}$ (x=1 and 2, n=1, 6, and 9 and m=12, 20, and 21), $Bi(OH)_3$, $BiCl_n^{+x}$ (x=1 and 2, n=1 and 2), $BiCl_n^{-x}$ (x=1, 2, and 3, n=4, 5 and 6) and $BiCl_3$.

Occurrences of native bismuth in Greece are found mainly in the Serbomacedonian, Rhodope and Atticocycladic massifs in Cu-Mo porphyries, skarns, carbonate replacement deposits and related vein stockworks, volcanic-hosted epithermal deposits and in shear-zone deposits (e.g., Plaka skarn, Lavrion, Greece, Voudouris et al., 2007 and references therein; Cook et al., 2009). In these deposits, the native bismuth is intergrown with bismuthinite, galena, Bi-sulfosalts (gustavite, lillianite, aikinite and cosalite), Bi-tellurides and electrum or occurs as inclusions in galena (Voudouris et al. 2007). Supergene alteration of native bismuth led to the formation of bismite and bismutite.

This study focuses on the Moutoulas deposit, an unexploited prospect, on Serifos Island, where native bismuth precipitated in clear quartz veins. In it, we investigate the

Always consult and cite the final, published document. See http:/www.minsocam.org or GeoscienceWorld

physicochemical controls on the precipitation of native bismuth as a retrograde skarn mineral and its subsequent supergene alteration. We introduce a new approach for the calculation of $Bi(OH)_2^+$ contours over temperature with the aim to predict the favourable conditions in which native bismuth precipitates. It is proposed that bismuth was transported as complexes involving hydroxyl and bicarbonate ions, e.g., $Bi(OH)_x^{3-x}(HCO_3)_y^{3-y}$ and that it deposited as native bismuth during mixing of the ore fluid with meteoric water.

Geological Setting

Serifos Island is part of the Attico-Cycladic massif of Greece, which includes three nappes: the lower Cycladic Basement Unit consisting of gneisses of Variscian ages (CB), the Cycladic Blueschist Unit (CBU) and the Upper Cycladic Unit (UCU) (Rabillard et al. 2015). The CB in Serifos comprises alternating hornblende-biotite and quartzo-feldspathic gneisses, intercalated with quartzites and marbles, and the CBU, amphibolites intercalated with gneisses and greenschists containing thinly-bedded dolomitic marbles. The latter unit represents a metamorphosed volcanosedimentary sequence developed along a Mesozoic continental margin. At least two Tertiary metamorphic events affected the CBU. The first event occurred between 53 and 40 Ma and was characterized by eclogite to blueschist facies conditions (T = 450-500ºC, P = 1.5±0.3 GPa, Brichau et al. 2010). This event was followed by a greenschist to amphibolite facies event (T = 670-700ºC and P = 0.4-0.7 GPa, Xypolias et al. 2012) that occurred between ≥ 25 and ~ 12 Ma (Bolhar et al. 2010). The UCU comprises an ophiolite nappe that was obducted in the Late Jurassic, and is overlain by unmetamorphosed sedimentary rocks (Bröcker and Franz 2005; Rabillard et al. 2015). The following lithotypes of UCU occur in Serifos (Fig. 1): calcitic marbles, ankerite-dolomite-

Always consult and cite the final, published document. See http:/www.minsocam.org or GeoscienceWorld

talc-goethite carbonate-replacement orebodies, meta-basites and serpentinites (Grasemann and Petrakakis 2007, Petrakakis et al. 2007). The lower Megalo Livadi detachment (ML) separates the CB from the CBU, and the upper Kavos Kiklopas detachment (KK) separates the CBU from the UCU (Grasemann et al., 2012; Ducoux et al. 2017, Fig. 1).

The Serifos pluton was emplaced at ~ 11.6 to 9.5 Ma in the CB and CBU rocks along the NE-SW trending ML detachment, creating a contact metamorphic aureole, 0.5 to 1 km in width (Fig. 1, Rabillard et al. 2015). I-type, hornblende-biotite granodiorite with subordinate tonalite intruded at its center, and granodiorite to S-type hornblende-biotite-allanite-zinnwaldite granite at its margins (Stouraiti and Mitropoulos 1999; Grasemann and Petrakakis 2007; Seymour et al. 2009). The pluton crystallized at a temperature of ~ 700º to 750 ºC and was emplaced at a pressure of 0.15 to 0.35 GPa (Seymour et al. 2009). Granodioritic to granitic apophyses, zoned pegmatites, aplites and dacitic dikes intruded the CBU rocks along NW-SE trending, counterclockwise reverse faults (Fig. 1). Their ages range from 8.2 to 8.7 Ma (Altherr et al., 1982), and they formed at $T \leq 650$ºC and P = 0.1-0.2 GPa (Stouraiti and Mitropoulos 1999; Seymour et al. 2009).

Pyroxene-garnet exoskarns occur in the CBU marbles and garnet- and pyroxene-garnet endoskarns in the pluton (Ducoux et al. 2017, Fig. 1). The exoskarns comprise diopside-hedenbergite, andradite, wollastonite, and magnetite and minor suanite ($Mg_2B_2O_5$) (Salemink 1985; Seymour et al. 2009, Fig. 1). Formation of ore minerals in the Serifos exoskarn began with the deposition of high-temperature magnetite at the contact of the pluton with the CBU (Fig. 1). Subsequent retrograde skarn formation at Moutoulas (~ 1 km from the pluton contact, Fig. 1) resulted in the precipitation of pyrite, sphalerite, chalcopyrite, galena and native bismuth. The mineralization takes the form of lenses up to 0.5×40×25 m in size that

Always consult and cite the final, published document. See http:/www.minsocam.org or GeoscienceWorld

mainly replaced the CBU marbles, and it is interpreted to represent an early carbonate replacement event (Seymour et al. 2009). Four major syntaxial quartz veins trending NNW-SSE (up to 100 m long and 0.5 m wide) cross-cut the CBU schists and marbles and are surrounded by alteration halos comprising an inner silica + sericite + pyrite ± calcite zone (replacing orthoclase and albite of the CBU schists), and an outer epidote ± chlorite, barite, pyrite and galena zone (Fig. 2a). The magnetite and sulfide ores underwent later supergene oxidation.

Analytical Methods

The ore minerals were identified using a combination of reflected light microscopy and X-ray diffraction (XRD) on a D8 Advance diffractometer (Bruker AXS) equipped with a LynxEye strip silicon detector. The X-ray diffractometer employed Ni-filtered CuKα radiation, a voltage of 35 kV, a 35 mA current, and 0.298º divergence and antiscatter slits. Random powder mounts of samples were scanned from 2º to 70º 2θ with a scanning step of 0.015º 2θ, and with 18.7 s count time per step, at the Research Laboratory of Minerals and Rocks, Department of Geology, University of Patras, Greece. Data were evaluated with the DIFFRACplus EVA v12.0® software and were compared with the PDF-2 database (ICDD, Newtown Square, PA, USA).

Ore mineral compositions were determined using a JEOL 8900 Superprobe equipped with energy and wavelength dispersive spectrometers (EDS and WDS, respectively) and an xClent system for ppm-level resolution, at the Microprobe Center of the Department of Earth and Planetary Sciences Department, McGill University. The operating conditions were an acceleration voltage of 15kV, a beam current of 10 nA, and counting time of 20 s for all

Always consult and cite the final, published document. See http:/www.minsocam.org or GeoscienceWorld

118 elements except Ag, As and Te for which the counting times were 100 s, and 50 s,
119 respectively. The standards used were natural chalcopyrite, tetrahedrite, tennantite, stibnite,
120 pyrite, sphalerite, and galena, synthetic CoNiAs, SnO_2 and CdTe, and the native metals Ag,
121 Au and Se. Minimum detection limits were 200 ppm for S, 300 ppm for Mn, Cd and Se, 400
122 ppm for Ag, Te and Au, 500 ppm for Zn, Fe and Co, 600 ppm for Sb and Bi, 700 ppm for Cu
123 and As and 2000 ppm for Pb.

124 Microthermometric measurements were performed on two doubly polished 50-100 μm
125 thick wafers in which clear quartz was in intergrowth with pyrite, sphalerite or native
126 bismuth. The Linkam MDSG600 heating-freezing stage coupled to a ZEISS microscope in
127 the Department of Earth Sciences and Resources, China University of Geosciences, Beijing,
128 China was used for this purpose. Temperatures were measured with an alumel-chromel
129 thermocouple and the readings were calibrated with synthetic inclusions at -56.6° (triple
130 point of CO_2), 0.0° (melting point of ice), and +374.1°C (critical point of H_2O). Freezing-
131 heating rates were maintained between 0.2° and 5°C/min and measurements were accurate
132 to ± 0.1°C. Microthermometric data were reduced using the FLINCOR software (Brown
133 1989).

134 A subset of the fluid inclusions was analyzed using Laser Raman spectroscopy. This was
135 done prior to microthermometric analysis in the Beijing Research Institute of Uranium
136 Geology, China. The inclusions were analyzed for the common gases, mono- and poly-atomic
137 ions and molecules via gas and ion chromatography. Gaseous composition was measured via
138 a LabRAM HR800 Raman spectroscopic microscope, with a laser beam spot size of ~ 1μm.
139 The instrument recorded peaks ranging from 100-4000 cm^{-1} with a spectral resolution of 1-2
140 cm^{-1}, and their peaks identified using the reference catalog of Frezzotti et al. (2012). The

Always consult and cite the final, published document. See http:/www.minsocam.org or GeoscienceWorld

141 relative concentrations (in mol %) of these species were calculated from the equations of
142 Frezzotti et al. (2012) and the cross-sectional scattering coefficients of Dhamelincourt et al.
143 (1979), using the LabSpec software. Liquid composition analysis was carried out with a
144 Shimadzu HIC-SP Super ion chromatograph on double distilled water leaches using the
145 method of Yardley et al. (1993). The analytical precision for all gases analyzed was ± 1%,
146 whereas for the cations and anions ±0.1 ppm.

147 Fifteen sulfide mineral samples were analyzed for their sulfur isotope compositions. Only
148 crystals of a given sulfide in textural equilibrium with contiguous crystals were selected for
149 analysis in order to be used for geothermometry. These crystals were handpicked after
150 examination under a binocular microscope to ensure textural equilibrium and a purity of ≥
151 98 %. Isotopic compositions of sulfur were analyzed with a VGMM602E double collector
152 mass spectrometer at the Chinese Academy of Geological Sciences (CAGS), Beijing, China.
153 Sulfur from vein pyrite, chalcopyrite, sphalerite, greenockite, and galena was released using
154 the method of Fritz et al. (1974). The sulfur isotopic ratios are reported in standard δ notation
155 per mil relative to V-CDT. Analytical precision was better than ± 0.2 per mil for $\delta^{34}S$. We
156 used the AlphaDelta software (Beaudoin and Therrien 2009) to compute the isotopic
157 fractionation factors and temperatures for mineral pairs in isotopic equilibrium. In addition,
158 we analyzed pyrite and galena for their lead isotope compositions. Lead isotopic
159 compositions were determined using an England Nu Plasma High Resolution type MC-ICP-
160 MS with standard NBS-981, following the method of Yuan et al. (2013). Long-term repeated
161 measurements of lead isotopic ratios of standard NBS981 yielded $^{206}Pb/^{204}Pb = 16.9397 \pm$
162 0.001 and $^{207}Pb/^{204}Pb = 15.4974 \pm 0.001$ (all errors are reported at ± 2σ).
163

Always consult and cite the final, published document. See http:/www.minsocam.org or GeoscienceWorld

The Moutoulas Mineralization

Examination of the quartz veins reveals four distinct paragenetic stages of hydrothermal mineralization which can be recognized on the basis of mineralogical and textural relations (Fig. 2b, Table 1). The stage I assemblage occupies the margins of the veins and is characterized by massive, brecciated aggregates of subhedral pyrite with intergrowths of minor arsenopyrite, sphalerite (X_{FeS}% = 20.7-25.8), chalcopyrite and pyrrhotite (Figs. 2b, 3a and b). Pyrite crystals incorporate appreciable amounts of Bi as submicroscopic grains of bismuthinite (Table 2). Stage II is represented by Bi- and Te-rich tetrahedrite-tennantite solid solutions ($X_{As\%}$ = 1.9 to 2.3) and sphalerite ($X_{FeS\%}$ = 13.8-18.7) filling brecciated pyrite (Fig. 3c, Table 2), as well as minor greenockite and gersdorffite. Frequently, tetrahedrite-tennantite is observed to have replaced pyrite from stage I (Fig. 3c). Stage III occurs towards the vein center and consists of Bi-bearing galena which intergrowns with fluorite and calcite and replaces stage I and II minerals (Fig. 3d, Table 2).

The stage IV assemblage develops in three sub-stages, as disseminations replacing stage III galena in the central parts of the veins (Figs. 2c, 3e and f, Tables 1, 2). Calcite, fluorite and barite also represent this stage. The early sub-stage includes euhedral acicular bismuthinite (Fig. 3e). The middle sub-stage comprises tellurides, including tetradymite, hessite, and melonite, and is succeeded by the late sub-stage which is dominated by native bismuth (Figs. 3e and f). In places, native bismuth replaced bismuthinite (Fig. 3f). During subsequent supergene alteration, mixtures of beyerite, bismutite and bismite replaced native bismuth (Figs. 2c, 3e, f and 4, Table 2). Covellite, cerussite, anglesite, chalcocite, goethite, azurite, and malachite also are products of this supergene stage (Table 1, data not shown).

Always consult and cite the final, published document. See http:/www.minsocam.org or GeoscienceWorld

Results

Fluid Inclusion Studies

Fluid inclusion data were obtained for two undeformed samples containing clear quartz and sphalerite; the data are for stages I to IV. The analysed fluid inclusions assemblages (FIA's) occur individually or as small randomly oriented clusters (4-10 μm in diameter). These inclusions are considered as primary in origin following the criteria of Roedder (1984). Their shapes include elliptical, negative crystal, and irregular forms without signs of necking down (Figs. 4a and b). Inclusions were considered to be secondary if they occur in planar arrays interpreted to be healed fractures that do not terminate at growth zones or grain boundaries (Fig. 4a and b).

At room temperature, only one type of fluid inclusions was recognized, namely L-V inclusions, consisting of aqueous liquid and vapor, with the liquid being dominant (accounting for ~ 90 vol. % of the total fluid inclusion volume; Table 3, Fig. 4b). Neither daughter crystals, trapped solids nor clathrates were observed. The temperature of initial melting of ice ranged from -23.8° to -21.1°C and the temperature of last melting of ice from -3.7° to -2.1°C (Table 3). Using the software FLINCOR (Brown 1989) for the system H_2O-NaCl (their initial melting temperatures are similar to the eutectic temperature of the system NaCl-H_2O), the corresponding salinities are 1.3 to 5.6 wt. % NaCl equivalent (Table 3, Fig. 5). The inclusions homogenize to liquid between 190° and ~ 250°C (Table 3, Fig. 5). As the pressure corresponding to the interpreted depth of emplacement of the Serifos pluton is interpreted to have been 3 to 12 km (Seymour et al., 2009), the trapping temperature of the inclusions was estimated to be ~ 5°C higher than the homogenization temperature (corrected by the FLINCOR software). In order to fully constrain the density and pressure of entrapment

Always consult and cite the final, published document. See http:/www.minsocam.org or GeoscienceWorld

(hydrostatic) of the fluid we made use of the Package FLUIDS (Bakker, 2012). The calculated hydrothermal trapping pressures for the L-V inclusions vary from 80 to 140 bars, and average 105 bars (st.d. = 10 bars). The fluid densities range from 0.84 to 0.90 g/ml.

Raman spectroscopy and gas chromatography

Laser Raman and bulk composition chromatographic analyses were conducted on four L-V fluid inclusions hosted by stage I and IV clear quartz that had been analyzed microthermometrically (Tables 4 and 5, Fig. 4b). Raman analyses reveal that the gaseous fluid phase is composed of H_2O, CO_2, O_2, H_2 and H_2S. The $\log X_{CO_2/H_2O}$, $\log X_{O_2/H_2O}$ and $\log X_{H_2S/H_2O}$ ratios range from of -1.0 to -0.8, -2.4 to -1.8, and -3.5 to -1.7, respectively. Also, in order to estimate temperature we have used the CO_2- and CO_2/H_2S-geothermometers of Arnórsson and Gunnlaugsson (1985) and Nehring and D'Amore (1984). The calculated temperatures for stages I and IV are 235° to 248°, and 190° to 197°C, respectively.

Bulk analyses of the liquid phase showed that it contained the cations Na^+, K^+, Mg^{2+}, Ca^{2+}, Si^{4+} and the anions Cl^-, SO_4^{2-} and HCO_3^-. Si^{4+} and HCO_3^- are the dominant ions in solution. These data allowed us to estimate the temperatures for the stages I and IV we used the Na-K-Ca geothermometer of Fournier and Truesdell (1973). The temperatures obtained were ~ 241° and 191°C to 195°C.

Isotope Geochemistry

Sulfur isotopes

Sulfur isotope analyses were conducted on pyrite, sphalerite, chalcopyrite, greenockite and galena (Table 6). The $\delta^{34}S_{V\text{-}CDT}$ isotopic values of stage I pyrite, sphalerite and chalcopyrite

Always consult and cite the final, published document. See http:/www.minsocam.org or GeoscienceWorld

range from 2.7 to 5.1 per mil. Values of $\delta^{34}S_{V\text{-}CDT}$ for stage II sphalerite and greenockite and III galena, were generally higher, 3.5, 5.5, and 5.0 to 5.6 per mil, respectively (Table 6). Temperatures of 249° ± 2°C and 226°C were calculated for stage I and stage II from the pyrite-sphalerite and sphalerite-greenockite isotopic pairs, respectively, utilizing the equations of Ohmoto and Rye (1979), Ohmoto and Lasaga (1982) and Li and Liu (2006). The calculated $\delta^{34}S_{H_2S}$ values of the mineralizing fluid range from 2.3 to 4.9 (stage I, pyrite, sphalerite, and chalcopyrite) 3.1 to 4.8 (stage II, sphalerite and greenockite) and 2.4 to 2.8 per mil (stage III, galena) (Table 6). These $\delta^{34}S_{H_2S}$ values reflect a dominantly magmatic source for sulfur for the ore fluids, i.e., the Serifos granodiorite.

Lead isotopes

Lead isotope data were obtained for stage I pyrite and stage III galena. Their $^{206}Pb/^{204}Pb$ and $^{207}Pb/^{204}Pb$ ratios range from 18.806 to 18.902 ± 0.001 and 15.653 to 15.702 ± 0.001 (Table 6). Our $^{206}Pb/^{204}Pb$ and $^{207}Pb/^{204}Pb$ values are very similar to those obtained by Stos-Gale (1992) from the Serifos granodiorite (Kefala site, i.e., 18.882 to 18.870 and 15.636 to 15.699) (Fig. 6).

Discussion

Physicochemical Conditions of Native Bismuth Formation

Physicochemical conditions of Moutoulas mineralization were estimated from phase stability relationships using SUPCRT92 (Johnson et al. 1992) with thermodynamic properties from the 2007 database (slop07.dat; Shock and Helgeson 1998). Reactions used to estimate these conditions and values of physicochemical parameters calculated using them are presented in

Always consult and cite the final, published document. See http:/www.minsocam.org or GeoscienceWorld

Table 7. The corresponding phase relationships are illustrated graphically on pH versus logfO_2 plots calculated for temperatures of 250° and 200°C (Figs. 7a and b). These temperatures represent those estimated previously for stage I and stage IV, respectively (Tables 3, 4, 5 and 6). All solids and gas species were considered behave ideally. Individual ion activity coefficients of dissolved species were calculated using the B-gamma extension of Helgeson et al. (1981) for an ionic strength (I) of 0.2.

The formation of sericite after orthoclase and albite in the inner alteration zone of the CBU schists require weakly acidic conditions during stage I (Reactions 1 to 3, Table 7). A $\log(\alpha_{K^+}/\alpha_{Na^+})$ value of 0.73, at 250°C, was calculated based on the equilibrium between orthoclase and albite (Reaction 3). The $\log(\alpha_{K^+}/\alpha_{H^+})$ and $\log(\alpha_{Na^+}/\alpha_{H^+})$ values obtained from Reactions 1 and 2 are 3.7 and 2.4, and so the calculated $\log\alpha_{Na^+}$ value is -0.47. The pH of the ore solution obtained from these values is 5.4.

A logfS_2 value of -13.8 ± 0.2 (PP-0.8, where PP is the pyrite-pyrrhotite buffer) was calculated for stage I from the pyrite and pyrrhotite equilibrium (Reaction 4, Table 7). The maximum X_{FeS} content of sphalerite coexisting with pyrite, for this stage is 25.8 % and the calculated logfS_2 value is -14.1 ± 0.2 (PP-1.1) based on the equation of Barton and Skinner (1979). Using compositional data for the gas phase in the fluid inclusions (Table 4, Reaction 5 in Table 7) and the equations of McCartney and Lanyon (1989), we were also able to calculate the corresponding logfO_2 (-39.2 or HM-2.1, where HM is the hematite-magnetite buffer) (Fig. 7a).

By stage IV, the temperature had decreased to 200°C, log fS_2 decreased to -16.5 ± 0.5 (PP-1.4) and logfO_2 to -43.5 (HM-3.5) (Fig. 7b). The value of logfS_2 was calculated from thermodynamic data for Reaction 6, which describes the replacement of bismuthinite by

Always consult and cite the final, published document. See http:/www.minsocam.org or GeoscienceWorld

native Bi, a common occurrence in late sub-stage IV. The value of log fO_2 was determined from compositional data for the gas phase in fluid inclusions as mentioned above for stage I (Table 7). The pH of the fluid (6.5) and the $\log\alpha_{HS^-(aq)}$ and $\log\alpha_{H2S(aq)}$ values (-2.9 and -3.7) were calculated using the equilibrium constants for Reactions 7, 8 and 9 for the $\log fO_2$ and $\log fS_2$ values referred to above (Table 7). A value of $\log fTe_{2(g)}$ (-17.0) was calculated from a combination of Reactions 10, 11 and 12. Increased $\log fTe_{2(g)}$ and $\log\alpha_{H2Te(aq)}$ and $\log\alpha_{HTe^-(aq)}$, values is suggested to be responsible for the formation of tellurides (e.g., hessite and tetradymite) via Reactions like 10 and 13 (Table 7).

During supergene alteration oxidation of native Bi (Reaction 14) produced $Bi(OH)^{2+}$ ions as the dominant dissolved species in solution. This reaction is promoted by higher $\log fO_2$ values (-32.5 or HM+10) and a further decrease of pH of 7.1 (Table 7). The formation of bismutite [$(BiO_2)_2CO_3$] and bismite (Bi_2O_3) was likely promoted by a Reaction similar to 15 (Table 7).

Source of Metals and Depositional Controls

Skarn formation, at Serifos, evolved from high-temperature magnetite ores to retrograde replacement and vein mineralization that culminated with the deposition of native bismuth. Figure 5 shows that the decrease in temperature from stage I (~250ºC) to stage IV (~190ºC) was accompanied by a roughly linear decrease in salinity from ≈ 5.7 to 1.3 wt. % NaCl equivalent. This trend suggests dilution of the ore fluid as a result of mixing with waters of meteoric origin. Mixing of the ore fluid with oxidizing meteoric waters is also suggested by the gas chemistry, i.e., an increase of the $\log X_{O2}/_{H2O}$ ratios from -3.4 to -2.8 (Pearce et al. 2004) (Table 4).

Always consult and cite the final, published document. See http:/www.minsocam.org or GeoscienceWorld

The sulfur isotope data yielded a narrow range of calculated $\delta^{34}S_{H2S}$ values, i.e., from 2.3 to 4.9 per mil (Table 6). Such $\delta^{34}S_{H2S}$ values reflect a dominantly magmatic source for the Bi-bearing mineralizing fluid. Further support is provided by the lead isotope data (Table 6) which suggest a mixed "Orogene" and "Upper Crust" source (Fig. 6). This implies that lead most probably derived from the Serifos pluton which concurs with the lead data provided by Stos-Gale (1992). Pyrite, tetrahedrite-tennantite solid solutions and galena from stages I, II and III of the Moutoulas mineralization contain Bi, indicating that this element was incorporated during retrograde skarn formation and at early stages of the vein-type mineralization. This is consistent with the fact that the Serifos pluton appears relative enriched in Bi towards its margins (e.g., up to ~ 60%, Seymour et al. 2009). The Serifos skarn resembles the Lavrion (Greece), Stan Terg (Kosovo) and Wittichen Schwarzwald (Germany) Bi-bearing skarns. In these skarns, Bi is thought to be related to fluids derived from or equilibrated with a granodiorite during the retrograde skarn phase (Fig. 6, Voudouris et al. 2008a and b; Kołodziejczyk et al. 2015; Staude et al. 2012).

The effects of temperature and pH on the solubility of $Bi(OH)^{2+}$ ions are summarized in a temperature versus pH plot (Fig. 8). Calculation of the contours of the mass of $Bi(OH)^{2+}$ in solution was based on Reaction 14 and the temperature, pH, $\log fO_2$, $\log fS_2$ and α_{H2S} values obtained for stages I and IV. Saturation of $Bi(OH)^{2+}$ is evident as the mass of $Bi(OH)^{2+}$ in solution decreases from T = 250º to T = 200ºC (Fig. 8). Here it is suggested that the conditions of stage I (lower pH and higher fS_2 and fO_2), favored the formation of Bi-enriched sulfides rather than the deposition of native bismuth. The proposed conditions for this stage lie within the stability fields of bismuthinite and pyrite which show a broad overlap (Fig. 7a). At these conditions, as the ore solution was undersaturated in Bi (Fig. 8), the available Bi cannot form

Always consult and cite the final, published document. See http:/www.minsocam.org or GeoscienceWorld

native bismuth and either is incorporated in the crystal lattice of the precipitated sulfides or forms submicroscopic grains within them (e.g., in pyrite and tetrahedrite, Table 2).

During stage IV native bismuth formed via Reaction 7 which was controlled by the interplay of six physicochemical parameters. Temperature decrease, pH neutralization, fTe_2 increase coupled with decrease of fS_2, α_{H2S} (X_{H2S} values decrease, Table 4) and fO_2 created a favorable environment for the precipitation of bismuthinite, then Bi-bearing tellurides and native bismuth (Fig. 7b). At these more reducing and less acidic conditions the solubility of bismuth decreased (e.g., the $\log\alpha_{Bi(OH)^{2+}}$ values increased from -14.0 to -11.2, Table 7, Fig. 8) thus leading to the precipitation of native bismuth.

We propose that variation of temperature, pH, $\log fS_2$, α_{H2S} $\log fO_2$ and $\log fTe_2$ was related to fluid-rock interaction and subsequent dilution of the ore fluid (Fig. 6). At Moutoulas open hydrothermal system, interaction of the Bi-bearing fluid with the intensely fractured CBU marbles also led to the enrichment of the mineralizing fluid in HCO_3^- ions (Table 5). Then supergene exposure and oxidation of the mineralization (e.g., $HCO_{3(aq)}^-$ anions required for reaction 15) may have resulted due to the intense exhumation and uplifting of the hydrothermal system (as it is suggested by Grasemann and Petrakakis 2007).

Implications

Herein we have reported on the first occurrence of native bismuth in the Serifos skarn. We recommend that proximity to the Serifos granodiorite, the development of magnetite ores and subsequent retrograde sulfide mineralization played important role in the precipitation of native bismuth. We propose that at such hydrothermal environment ($T \approx 200°C$) there are six

Always consult and cite the final, published document. See http:/www.minsocam.org or GeoscienceWorld

parameters, i.e., temperature, pH, logfS_2, α_{H_2S}, logfO_2 and logfTe_2 that may lead to native bismuth precipitation.

Wall-rock interaction and dilution of the Bi-bearing magmatic fluid, i.e., containing $Bi(OH)_2^{+}{}_{(aq)}$ with meteoric waters, promoted its saturation (Fig. 8) as they facilitated to decrease the mass of $Bi(OH)^{2+}$ ions in solution. We also propose that the formation of $Bi(OH)_x{}^{3-x}(HCO_3)_y{}^{3-y}$ complexes could play an important role on transporting this strategic element during wall-rock interaction. Destabilization of these complexes during dilution of the ore fluid via a probable reaction could be a mechanism controlling native bismuth precipitation:

$$Bi(OH)_2(HCO_3)_{(aq)} = Bi(OH)_2^{+}{}_{(aq)} + HCO_3^{-}{}_{(aq)} = Bi_{(s)} + 2H_2O_{(l)} + 2CO_{2(g)}.$$

Acknowledgements: We kindly thank D. Katsikis for his assistance with sampling in the Moutoulas mine. Critical comments from J. Mavrogenes, P. Voudouris, and the Associate Editor J. Roberge, as well as an anonymous reviewer are gratefully acknowledged.

Always consult and cite the final, published document. See http:/www.minsocam.org or GeoscienceWorld

References

Altherr, R., Kreuzer, H., Wendt, I., Lenz, H., Wagner, G.A., Keller, J., Harre, W., and Hohndorf, A. (1982) A late Oligocene/Early Miocene high temperature belt in the Attico-Cycladic crystalline complex (SE Pelagonia, Greece). Geologisches Jahrbuch, 23, 971-164.

Afifi, A.M., Kelly, W.C., and Essene, E.J. (1988) Phase relations among tellurides, sulfides, and oxides: I. Thermochemical data and calculated equilibria. Economic Geology, 83, 377-294.

Arnórsson, S., and Gunnlaugsson, E. (1985) New gas geothermometers for geothermal exploration-Calibration and application. Geochimica and Cosmochimica Acta, 49, 1307-1325.

Bakker, R.J. (2012) Package FLUIDS. Part 4: Thermodynamic modelling and purely empirical equations for H_2O-NaCl-KCl solutions. Mineralogy and Petrology, 105, 1-29.

Barton, P.B.Jr, and Skinner, B.J. (1979) Sulfide mineral stabilities. In, Barnes, H.L., (Ed), Geochemistry of the hydrothermal ore deposits, 3rd Edition. Wiley, J., and Sons, New York, pp. 236-333.

Beaudoin, G., and Therrien, P. (2009) The updated web stable isotope fractionation calculator: In De Groot PA (ed), Handbook of stable isotope analytical techniques, Volume II, Elsevier, 1120-1122.

Bolhar, R., Ring, U., and Allen, C.M. (2010) An integrated zircon geochronological and geochemical investigation into the Miocene plutonic evolution of the Cyclades, Aegean

383 Sea, Greece: Part 1: geochronology. Contributions to Mineralogy and Petrology, 160,
384 719-742.
385 Brichau, S., Thomson, S.N., and Ring, U. (2010) Thermochronometric constraints on the
386 tectonic evolution of the Serifos detachment, Aegean Sea, Greece. International Journal
387 of Earth Sciences, 99, 379-393, DOI 10.1007/s00531-008-0386-0.
388 Bröcker, M., and Franz, L. (2005) P-T conditions and timing of metamorphism at the base
389 of the Cycladic Blueschist unit, Greece: The Panormos window on Tinos re-visited.
390 Neues Jahrbuch für Mineralogie Abhandlungen, 181, 91-93.
391 Brown, P.E. (1989) FLINCOR: A microcomputer program for the reduction and
392 investigation of fluid inclusion data. American Mineralogist, 74, 1390-1393.
393 Chalkias, S., and Vavelidis, M. (1998) Interpretation of lead-isotope data from Greek Pb-Zn
394 deposits, based on an empirical two-stage model. Bulletin of Geological Society of
395 Greece, 23,177-193.
396 Cook, N.J., Ciobanu, C.L., Spry, P.G., Voudouris, P., and the participants of the IGCP-486
397 (2009) Understanding gold-(silver)-telluride-(selenide) mineral deposits. Episodes, 32,
398 249-263.
399 Dhamelincourt, P., Beny, J.M., Dubessy, J., and Poty, B. (1979) Analyse d' inclusions fluids
400 à la microsonde mole à effet Raman. Bulletin Mineralogie, 102, 600-610.
401 Ducoux, M., Branquet, Y., Jolivet, L., Arbaret, L., Grasemann, B., Rabillard, A., Gumiaux,
402 C., Drufin, S. (2017) Synkinematic skarns and fluid drainage along detachments: The
403 West Cycladic Detachment System on Serifos Island (Cyclades, Greece) and its related
404 mineralization. Tectonophysics, 695, 1-26.

Always consult and cite the final, published document. See http:/www.minsocam.org or GeoscienceWorld

405 Etschmann, B.E., Liu, W., Pring, A., Grundler, P.V., Tooth, B., Borg, S., Testemale, D.,
406 Brewe, D., and Brugger, J. (2016) The role of Te (IV) and Bi(III) chloride complexes
407 in hydrothermal mass transfer: an X-ray absorption spectroscopic study. Chemical
408 Geology, 425, 37-51.
409 Frezzotti, M.L., Tecce, F., and Casagli, A. (2012) Raman spectroscopy for fluid inclusion
410 analysis. Journal of Geochemical Exploration, 112, 1-20.
411 Fritz, P., Drimmie, R.J., and Norwick, K. (1974) Preparation of sulfur dioxide for mass
412 spectrometer analysis by combustion of sulfide with copper oxide. Analytical
413 Chemistry, 76, 164-166.
414 Grasemann, B., and Petrakakis, K. (2007) Evolution of the Serifos metamorphic complex.
415 In: Lister, G., Forster, M., Ring, U. (Eds), Inside the Aegean Metamorphic Core
416 Complexes. Journal of the Virtual Explorer, 28, 1-18.

417 Grasemann, B., Schneider, D.A., Stockli, D.F., and Iglseder, C. (2012) Miocene bivergent
418 crustal extension in the Aegean: Evidence from the western Cyclades (Greece),
419 Lithosphere, 4(1), 23-39, doi:10.1130/L164.1.
420 Helgeson, H.C., Kirkham, D.H., and Flowers, G.C. (1981) Theoretical prediction of the
421 thermodynamic behavior of aqueous electrolytes at high pressures and temperatures,
422 Calculation of activity coefficients, osmotic coefficients, and apparent molal and
423 standard and relative partial molal properties to 600°C and 5kb. American Journal of
424 Science, 281, 1249-1516.
425 Henley, R.W., Mavrogenes, J.A., and Tanner, D. (2012) Sulfosalt melts and heavy metal (As-
426 Sb-Bi-Sn-Pb-Tl) fractionation during volcanic gas expansion: the El Indio (Chile)
427 paleo-fumarole. Geofluids, DOI: 10.1111/j.1468-8123.2011.00357.x.

Always consult and cite the final, published document. See http:/www.minsocam.org or GeoscienceWorld

Johnson, J.W., Oelkers, E.H., and Helgeson, H.C. (1992) SUPCRT92, A software package for calculating the standard molal thermodynamic properties of minerals, gases, aqueous species and reactions from 1 to 5000 bars and 0º to 1000ºC. Computer Geoscience, 18, 899-947.

Kołodziejczyk, J., Pršek, J., Melfos, V., Voudouris, P., Maliqi, F., and Kozub-Budzyń, G. (2015) Bismuth minerals from the Stan Terg deposit (Trepça, Kosovo). Mineralogical contribution to the evolution of the deposit. Neues Jahrbuch fur Mineralogie, 192, 317-333.

Li, Y., and Liu, J. (2006) Calculation of sulfur isotope fractionation in sulfides. Geochimica et Cosmochimica Acta, 70, 1789-1795.

Mavrogenes, J.A., Henley, R.W., Reyes, A.C., and Berger, B. (2010) Sulfosalt melts: evidence of high temperature vapor transport of metals in the formation of high sulfidation lode gold deposits. Economic Geology, 105, 257-262.

McCartney, R.A., and Lanyon, G.W. (1989) Calculations of steam fractions in vapor-dominated geothermal systems using an empirical method. In l4th Annual Workshop on Geothermal Reservoir Engineering, Stanford, p. 155-161.

Nehring, N.L., and D'Amore, F. (1984) Gas chemistry and thermometry of the Cerro Prieto, Mexico, geothermal field. Geothermics, 13, 75-89.

Ohmoto, H., and Lasaga, A.C. (1982) Kinetics of reactions between aqueous sulfates and sulfides in hydrothermal systems. Geochimica et Cosmochimica Acta, 46, 1727-1745.

Ohmoto, H., and Rye, R.O. (1979) Isotopes of sulfur and carbon. In: Barnes, H.L. (ed.) Geochemistry of the hydrothermal ore deposits, 3rd Edition, Wiley J and Sons, New York, p. 509-567.

Always consult and cite the final, published document. See http:/www.minsocam.org or GeoscienceWorld

Pearce, J.A., Czernichowski-Lauriol, I., Lombardi, S., Brune, S., Nador, A., Baker, J., Pauwels, H., Hatziyannis, G., Beaubien, S., and Faber, E. (2004) A review of natural CO_2 accumulations in Europe as analogues for geological sequestration: Geological Society, London, Special Publication, 233, 29-41.

Petrakakis, K., Zamoyli, A., Iglseder, C., Rambousek, C., Grasemann, B., Dragamits, E., and Photiadis, A. (2007) Geological map of Serifos. 1:50.000. Geological map of Greece, Institute of Geological and Mineralogical Exploration, Athens, Greece.

Rabillard, A., Arbaret, L., Jolivet, L., Le Breton, N., Gumiaux, C., Augier, R., and Grasemann, B. (2015) Interactions between plutonism and detachments during metamorphic core complex formation, Serifos Island (Cyclades, Greece). Tectonics, 34, 1080-1106, DOI: 10.1002/2014TC003650.

Roedder, E. (1984) Fluid inclusions. Reviews in Mineralogy, 12, p. 550.

Salemink, J. (1985) Skarn and ore formation at Serifos, Greece as a consequence of granodiorite intrusion, 232 p. PhD thesis, Geology Ultraiectina.

Seymour, K., Zouzias, D., Tombros, S.F., and Kolaiti, E. (2009) The geochemistry of the Serifos pluton and associated iron oxide and base metal sulphide ores: Skarn or metamorphosed exhalite deposits? Neues Jahrbuch für Mineralogie Abhandlungen, 186, 249-270, DOI: 10.1127/0077-7757/2009/0143.

Shock, E.T., and Helgeson, H.C. (1998) Calculation of the thermodynamic and transport properties of aqueous species at high pressures and temperatures, Correlation algorithms for ionic species and equation of state prediction to 5 kb and 1000 °C. Geochimica et Cosmochimica Acta, 52, 2009-2036.

Always consult and cite the final, published document. See http:/www.minsocam.org or GeoscienceWorld

473 Simon, G., and Essene, E.J. (1996) Phase relations among selenides, sulfides, tellurides, and
474 oxides: I. Thermodynamic properties and calculated equilibria. Economic Geology, 91,
475 1183-1208.
476 Skirrow, R.G., and Walshem, J.L. (2002) Reduced and oxidized Au-Cu-Bi iron oxide
477 deposits of the Tennant Creek Inlier, Australia: an integrated geologic model.
478 Economic Geology, 97, 1167-1202.
479 Staude, S., Werner, W., Mordhorst, T., Wemmer, K., Jacob, D.E., and Markl, G. (2012)
480 Multi-stage Ag-Bi-Co-Ni-U and Cu-Bi vein mineralization at Wittichen, Schwarzwald,
481 SW Germany: Geological setting, ore mineralogy, and fluid evolution. Mineralium
482 Deposita, 47, 251-276, DOI 10.1007/s00126-011-0365-4.
483 Stos-Gale, A.Z. (1992) Application of lead isotope analysis to provenance studies in
484 archaeology. 303 p. PhD thesis University of Oxford.
485 Stouraiti, C., and Mitropoulos, P. (1999) Variation in amphibole composition from the
486 Serifos intrusive complex (Greece), under magmatic and hydrothermal alteration
487 conditions. An application of hornblende geobarometry. Bulletin of Geological Society
488 of Greece, 33, 39-50.
489 Tooth, B., Ciobanu, C.L., Green, L., O'Neill, B., and Brugger, J. (2011) Bi-melt formation
490 and gold scavenging from hydrothermal fluids: an experimental study. Geochimica et
491 Cosmochimica Acta, 75, 5423-5443.
492 Tooth, B., Brugger, J., Ciobanu, C., and Liu, W. (2008) Modeling of gold scavenging by
493 bismuth melts coexisting with hydrothermal fluids. Geology, 36, 815-818.

Always consult and cite the final, published document. See http:/www.minsocam.org or GeoscienceWorld

494 Voudouris, P., Spry, P.G., Melfos, V., Alfieris, D. (2007) Tellurides and bismuth sulfosalts
495 in gold occurrences of Greece: mineralogy and genetic considerations. Geological
496 Survey of Finland Guide 53, 85-94.
497 Voudouris, P., Melfos, V., Spry, P.G., Bonsall, T., Tarkian, M., Economou-Eliopoulos, M.
498 (2008a) Mineralogy and fluid inclusion constraints on the evolution of the Plaka
499 intrusion-related ore system, Lavrion, Greece. Mineralogy and Petrology, 93, 79-110.
500 Voudouris, P., Melfos, V., Spry, P.G., Bonsall, T., Tarkian, M., Solomos, C. (2008b)
501 Carbonate-replacement Pb-Zn-Ag±Au mineralization in the Kamariza area, Lavrion,
502 Greece: Mineralogy and thermochemical conditions of formation. Mineralogy and
503 Petrology, 94, 85-106.
504 Xypolias, P., Iliopoulos, I., Chatzaras, V., and Kokkalas, S. (2012) Subduction and
505 exhumation related structures in the Cycladic Blueschists: insights from Evia Island
506 (Aegean region, Greece). Tectonics, 31, TC2001, doi: 10.1029/2011TC002946.
507 Yardley, B.W.D., Banks, D.A., Bottrell, S.H. (1993) Post-metamorphic gold-quartz veins
508 from N.W. Italy: the composition and origin of the ore fluid. Mineralogical Magazine,
509 57, 407-422.
510 Yuan, H., Chen, K., Zhian, B., Zong, C., Dai, M., Fan, C., and Yin, C. (2013) Determination
511 of lead isotope compositions of geological samples using femtosecond laser ablation
512 MC-ICPMS. Chinese Science Bulletin, 58, 3914-3921.
513 Zartman, R.E., and Doe, B.R. (1981) Plumbotectonics. The Model. Tectonophysics, 75, 135-
514 162.

Always consult and cite the final, published document. See http:/www.minsocam.org or GeoscienceWorld

515 Zhou, H., Sun, X., Fu, Y., Lin, H., and Jiang, L. (2016) Mineralogy and mineral chemistry
516 of Bi-minerals: Constraints on ore genesis of the Beiya giant porphyry-skarn gold
517 deposit, southwestern China. Ore Geology Reviews 79, 408-424.

Always consult and cite the final, published document. See http:/www.minsocam.org or GeoscienceWorld

518 **Figure Captions**

519 Fig. 1. Simplified geological map of Serifos Island with the locations of magnetite exo- and
520 endo-skarns, hematite ores and sulfides (modified after Salemink 1985; Grasemann and
521 Petrakakis 2007 and Rabillard et al. 2015). The triangle represents the location of Fig. 2.

522 Fig. 2. (a) A view of a sheared quartz vein at the interface between CBU schists and marbles
523 containing the Bi-bearing assemblages studied. A bleached alteration halo is also evident.
524 Also shown are the sampling sites (b and c).
525 (b) A hand specimen of the vein containing pyrite (Py) and galena (Gn) (scale bar = 1 cm).
526 (c) Native bismuth (Bi) rimmed by a supergene assemblage (S) of beyerite, bismutite and
527 bismite (scale bar = 5 cm).

528 Fig. 3. Reflected light and back-scattered electron images of:
529 (a). Stage I pyrite (Py) and sphalerite (Sp1) (scale bar = 1 mm),
530 (b). Stage I pyrite (Py) with pyrrhotite (Po) (Reaction 4, Table 7, scale bar = 1 μm),
531 (c). Stage II sphalerite (Sp2) and tetrahedrite-tennantite solid solutions (Tnt) filling fractures
532 in brecciated stage I pyrite (Py) (scale bar = 1 μm),
533 (d). Stage III galena (Gn) after stage I pyrite (Py) (scale bar = 100 μm),
534 (e). Late sub-stage IV native Bi (Bi) that replaced early sub-stage IV bismuthinite (Bst)
535 (Reaction 7, Table 7). Both minerals were partially oxidized to bismite (Bsm) (scale bar
536 = 500 μm),
537 (f). Late sub-stage IV native Bi (Bi) after early sub-stage IV bismuthinite (Bst) and middle-
538 sub-stage tetradymite. Native Bi was oxidized to bismite (Bsm) (Reactions 14 and 15,
539 Table 7) (scale bar = 20 μm).

540 Fig. 4. Photomicrographs of multiple fluid inclusion assemblages:

(a). Primary two-phase L-V (P) and secondary L-V (S) inclusions. The primary inclusions occur individually or as small, randomly oriented clusters, whereas the secondary fluid inclusions form trails that are aligned along fractures and terminate at crystal growth surfaces (scale bar = 25 μm),

(b). Detail of (a) showing the primary inclusions with low V-L ratios (vapor bubble occupies up to ~ 20 vol %) used for Raman spectroscopy (scale bar = 100 μm),

Fig. 5. Liquid-vapor trapping temperature versus salinity plot in the system NaCl-H_2O.

Fig. 6. A plot of $^{206}Pb/^{204}Pb$ versus $^{207}Pb/^{204}Pb$ using age-corrected data. The galena crystals analyzed in this study plot between the "Orogene" and "Upper Crust" curves. The "Upper Crust", "Orogene" and "Mantle" were based on the model of Zartman and Doe (1981). Also shown are samples of galena from the Kefala pluton (Stos-Gale, 1992) and the Moutoulas mineralization (Chalkias and Vavelidis, 1998)

Fig. 7. (a). LogfO_2 versus pH plot for 250ºC, representing stage I of the Moutoulas skarn and vein mineralization. The dashed lines define the stability fields for pyrite (FeS_2), pyrrhotite (FeS), hematite (Fe_2O_3) and magnetite (Fe_3O_4). The Fe-S-O mineral boundaries are shown for $\Sigma S = 0.1$ moles/kg H_2O. Also shown are the sulfur species in the system H-S-O (dotted lines), the stability boundary for muscovite-K-feldspar (short-dash-dotted line), and the stability fields for bismuthinite, maldonite (Au_2Bi), and native bismuth (thick solid lines) fields,

(b). LogfO_2 versus pH plot for 200ºC, representing stage IV of the Moutoulas skarn mineralization. The dashed lines define the stability fields for pyrite (FeS_2), pyrrhotite (FeS), hematite (Fe_2O_3) and magnetite (Fe_3O_4). The Fe-S-O mineral boundaries are shown for $\Sigma S = 0.1$ moles/kg H_2O. The thin dotted and thin solid lines are the calculated contours

Always consult and cite the final, published document. See http:/www.minsocam.org or GeoscienceWorld

564 for the sulfur and tellurium species in solution. Also shown are the stability boundaries
565 for kaolinite-sericite (short-dash-dotted line) and anglesite-galena (short-dotted lines) and
566 the stability fields for the sulfur species in the system H-S-O (dotted lines), and
567 bismuthinite-native bismuth (thick solid lines). Data from Barton and Skinner (1979),
568 Simon and Essene (1996), Afifi et al. (1988), Skirrow and Walshe 2002, Tooth et al.
569 (2008, 2011) and Staude et al. (2012) were employed to calculate the Bi mineral stability
570 fields in the two diagrams.

571 Fig. 8. Temperature versus pH plot summarizing changes in solubility of $Bi(OH)^{2+}$ ions
572 (Squares represent stage I and cycles stage IV). Calculation of the contours of mass in
573 solution of $Bi(OH)^{2+}$ (in ppm) was based on Reaction 14, for $\log\alpha_{H2S} = -3.7$ and $\log\alpha_{\Sigma S} =$
574 -3.0, and the $\log fO_2$ and $\log fS_2$ values obtained for stages I and IV. Also shown are the
575 stability boundary bismuthinite, and native bismuth (thick solid line).

576

Always consult and cite the final, published document. See http:/www.minsocam.org or GeoscienceWorld

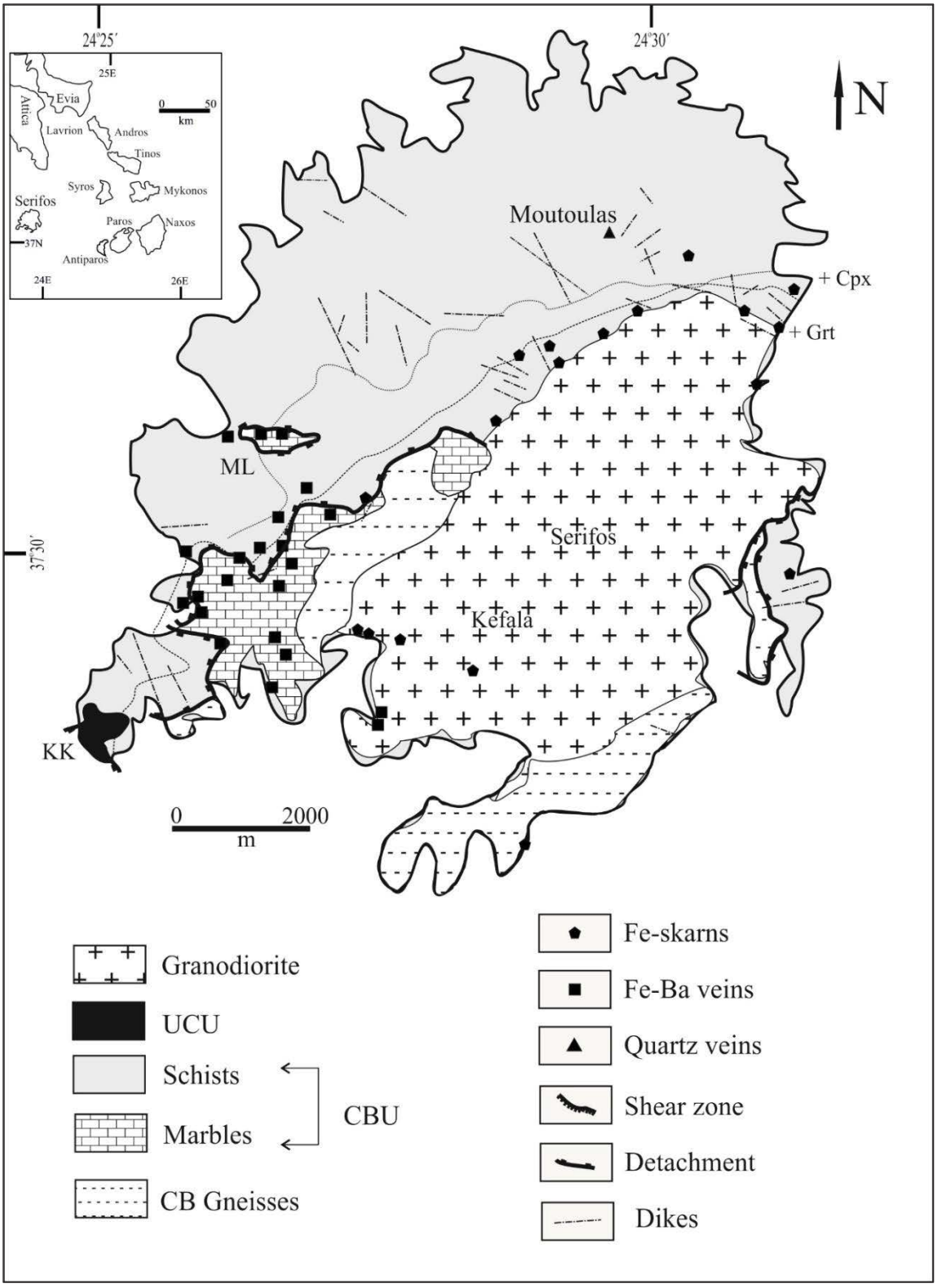

577

578 **Fig. 1.**

Always consult and cite the final, published document. See http:/www.minsocam.org or GeoscienceWorld

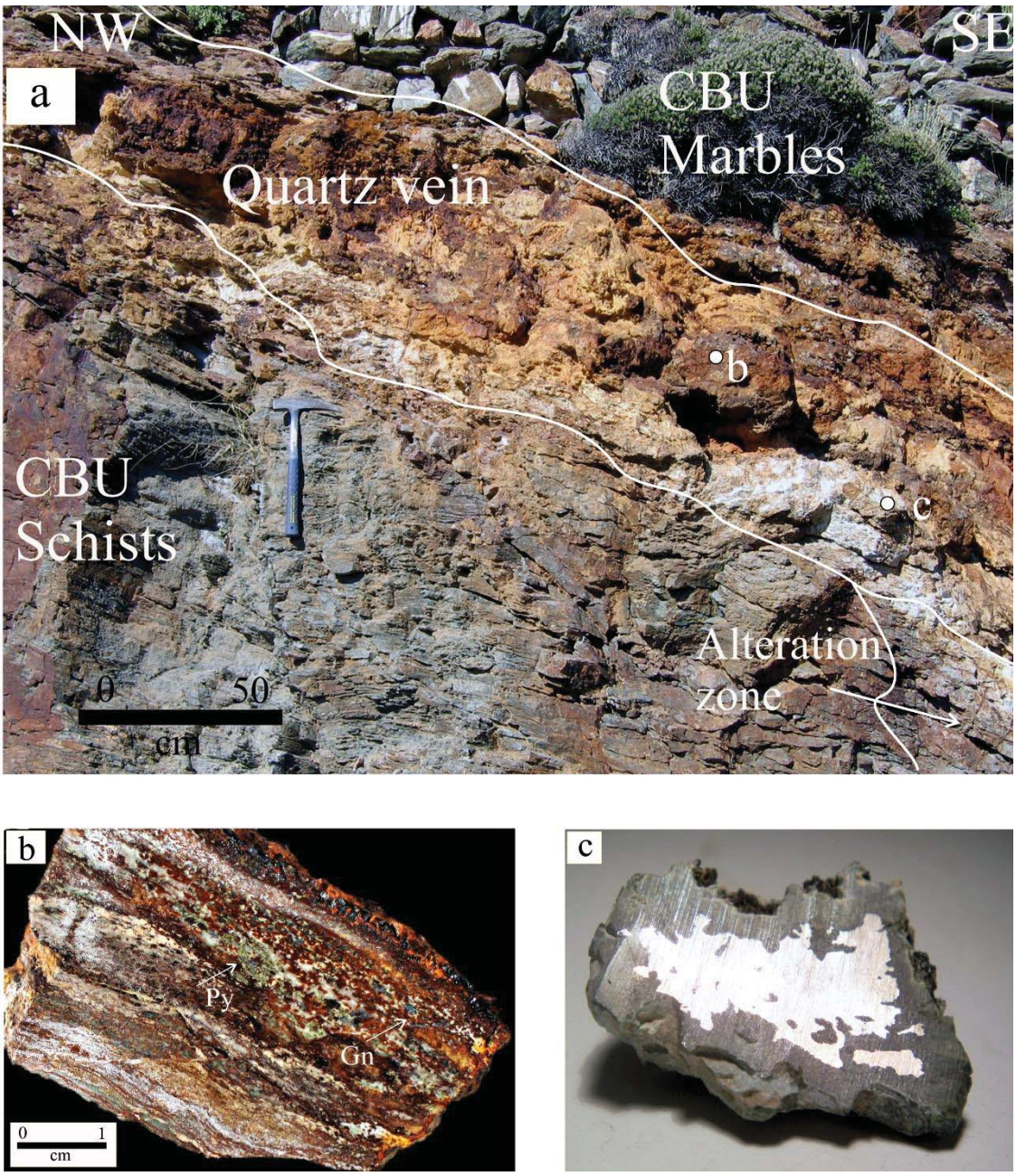

579

580

581 **Fig. 2. Fitros et al. (2016).**

582

583

584

Always consult and cite the final, published document. See http:/www.minsocam.org or GeoscienceWorld

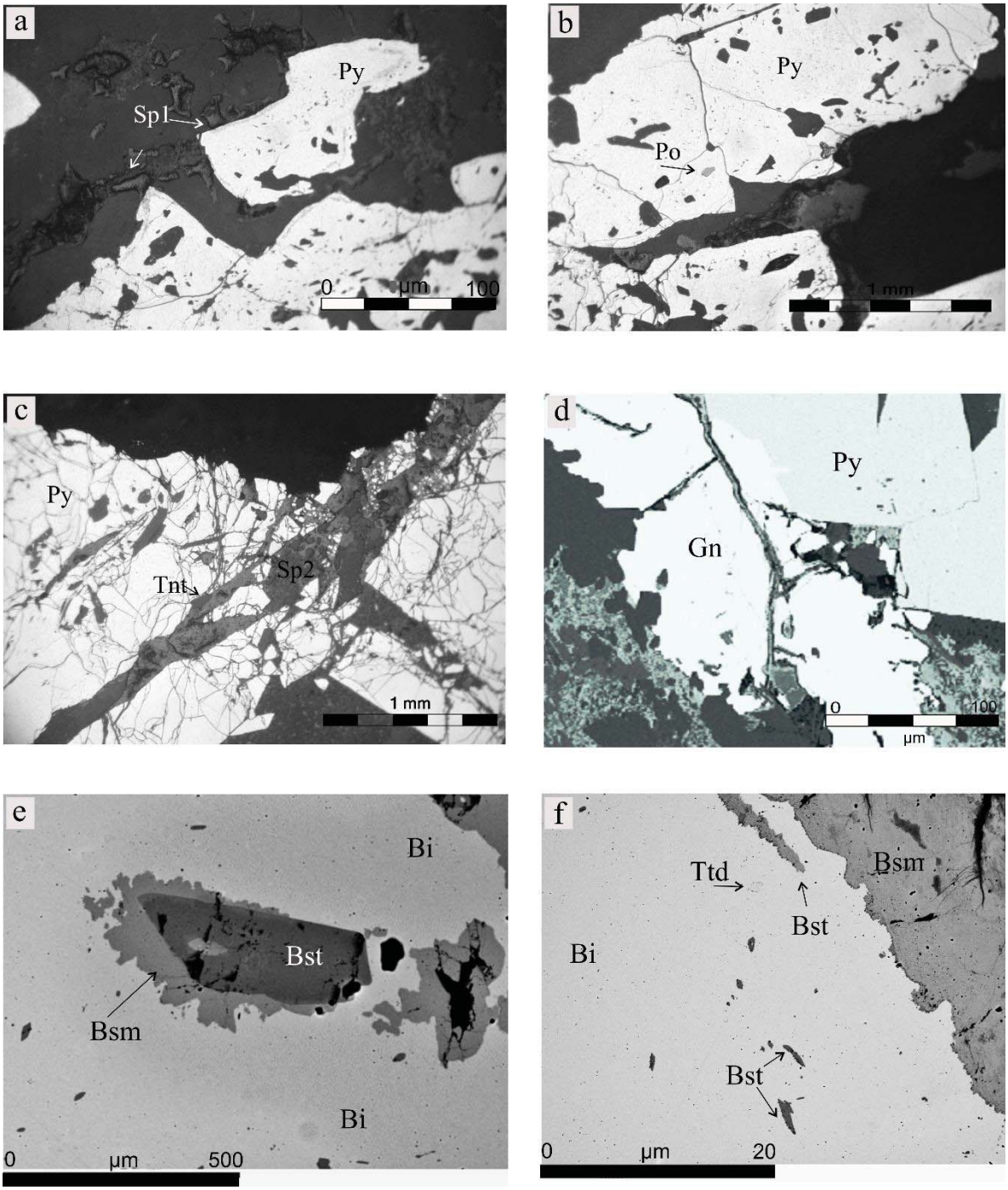

585

586 **Fig. 3 (a, b, c, d, e and f). Fitros et al. (2016).**

587

588

Always consult and cite the final, published document. See http:/www.minsocam.org or GeoscienceWorld

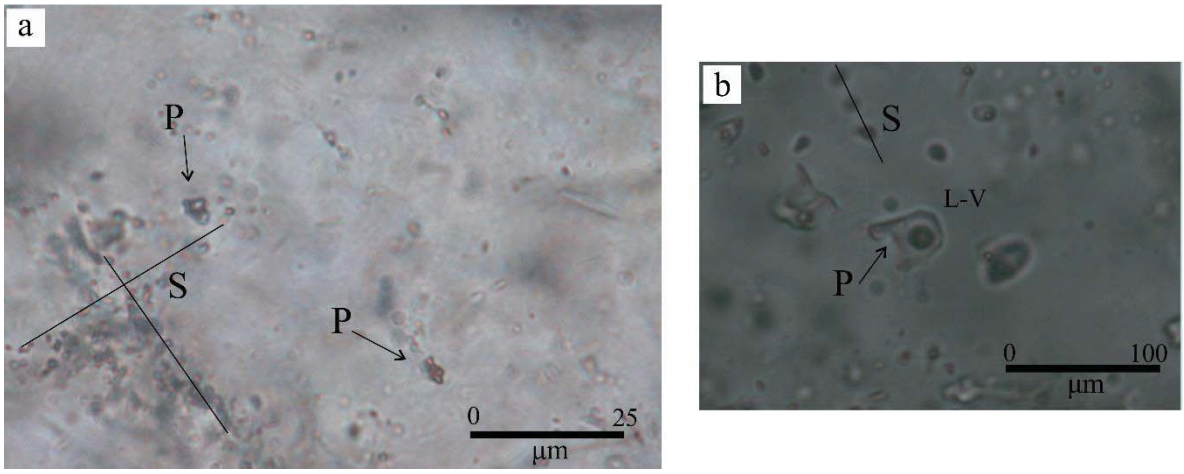

Fig. 4 (a and b). Fitros et al. (2016).

Always consult and cite the final, published document. See http:/www.minsocam.org or GeoscienceWorld

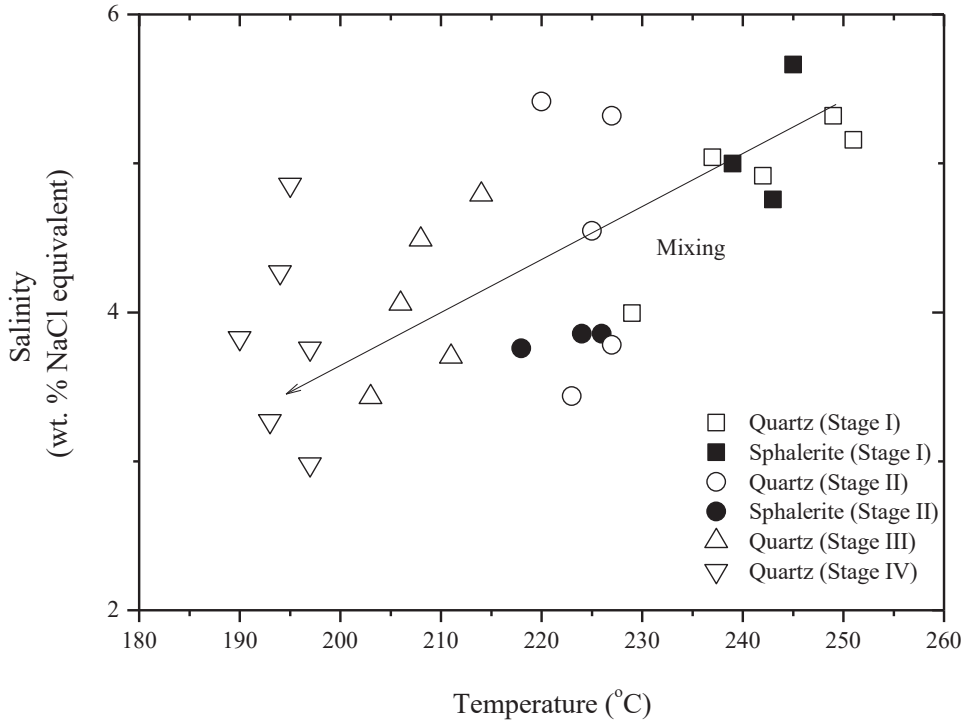

602

603 **Fig. 5. Fitros et al. (2016).**

604

605

606

Always consult and cite the final, published document. See http:/www.minsocam.org or GeoscienceWorld

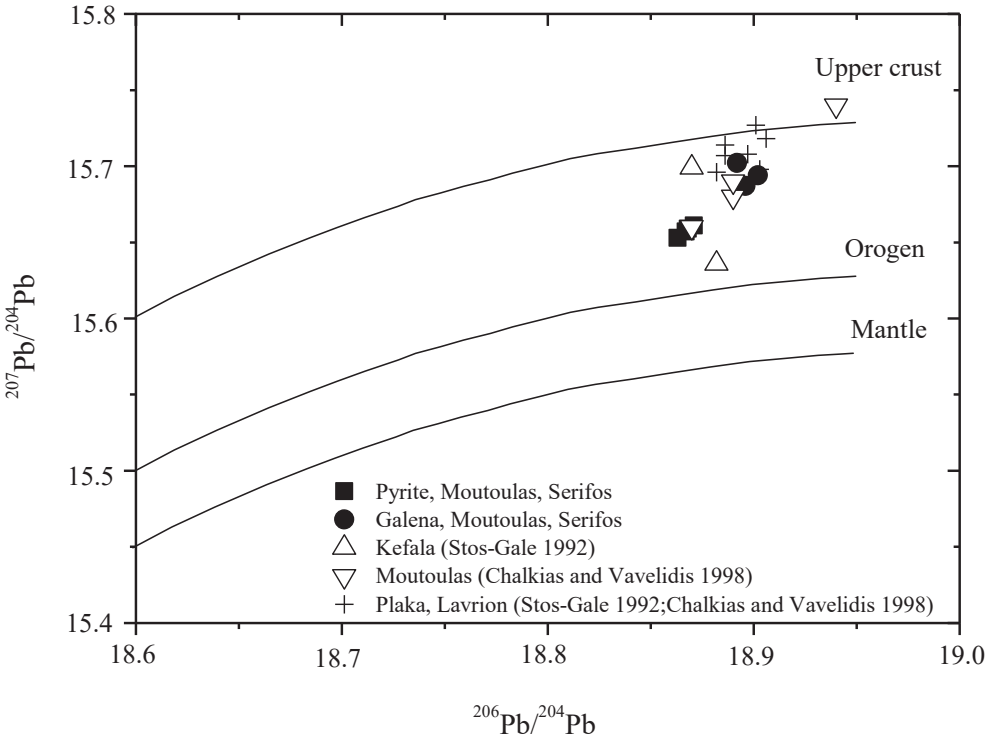

607

608 **Fig. 6. Fitros et al. (2016).**

609

610

611

612

613

614

615

616

617

618 a.

Always consult and cite the final, published document. See http:/www.minsocam.org or GeoscienceWorld

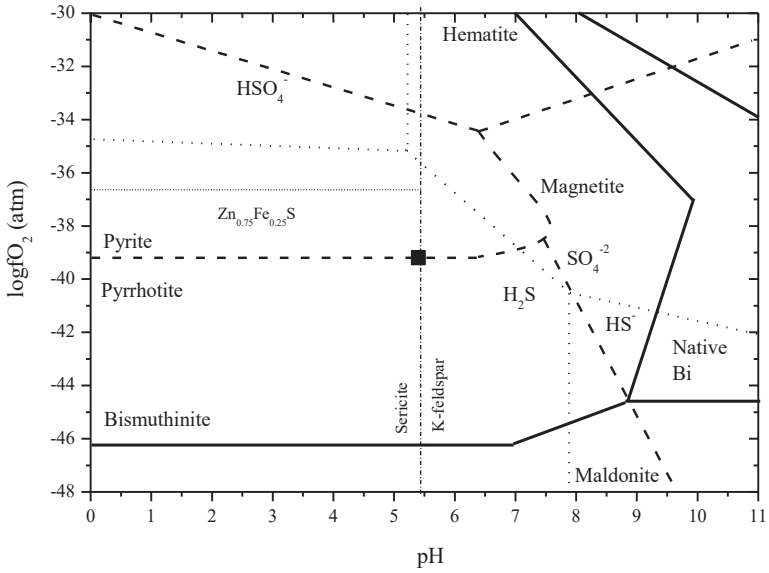

619

620 b.

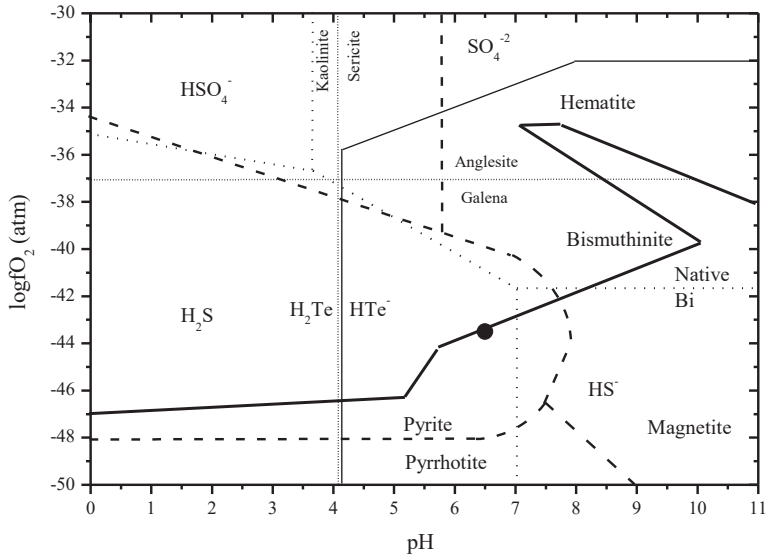

621

622 **Fig. 7. (a and b). Fitros et al. (2016).**

623

Always consult and cite the final, published document. See http:/www.minsocam.org or GeoscienceWorld

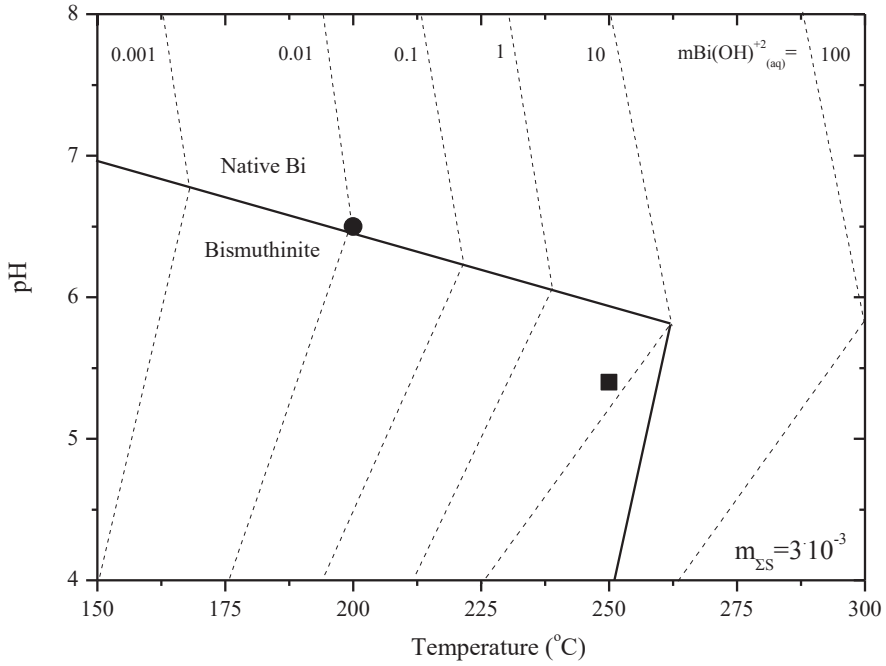

624

625 **Fig. 8. Fitros et al. (2016).**

626

Always consult and cite the final, published document. See http:/www.minsocam.org or GeoscienceWorld

This is a preprint, the final version is subject to change, of the American Mineralogist (MSA)
Cite as Authors (Year) Title. American Mineralogist, in press.
(DOI will not work until issue is live.) DOI: http://dx.doi.org/10.2138/am-2017-6125

627 Table 1. Ore paragenesis and vein fill minerals from Moutoulas area, Serifos.

Mineral stages	Stage I	Stage II	Stage III	Stage IV[A]	Supergene stage
T (°C)	250			200	
Clear quartz	▬▬▬	▬▬▬	▬▬	▬	
Calcite			▬▬	▬▬	
Beyerite			▪	▬▬	▬▬
Barite				▬	
Fluorite			▬	▪	
Pyrite	▬				
Sphalerite	▬[1]	▪[2]			
Chalcopyrite	▪				
Arsenopyrite	▪				
Pyrrhotite	▪				
Tetrahedrite-Tennantite		▬[3]			
Greenockite		▪			
Gersdorffite		▪			
Galena			▬▬		
Bismuthinite[E]				▪	
Tetradymite[M]				▪	
Hessite[M]				▪	
Melonite[M]				▪	
Native Bismuth[L]				▪	▬
Bismutite					▬▬
Bismite					▬▬
Covellite					▪
Cerussite					▪
Anglesite					▪
Chalcocite					▪
Goethite					▪
Azurite					▪
Malachite					▪

628 Chemical formulae: Bismuthinite (Bi_2S_3), Tetradymite (Bi_2Te_2S), and Melonite ($NiTe_2$),
629 Beyerite ($Ca(BiO)_2(CO_3)_2$), Bismutite ($Bi_2O_2(CO_3)$), Bismite (Bi_2O_3).
630 The boxes represent the abundance.
631 [1]$X_{FeS\%}$ = 25.8, [2]$X_{FeS\%}$ = 13.8, [3]X_{As} = 1.9 to 2.3.
632 [A]Stage IV composes of three sub-stages, i.e., [E]Early, [M]Middle, and [L]Late sub-stage.
633

Always consult and cite the final, published document. See http:/www.minsocam.org or GeoscienceWorld

This is a preprint, the final version is subject to change, of the American Mineralogist (MSA)
Cite as Authors (Year) Title. American Mineralogist, in press.
(DOI will not work until issue is live.) DOI: http://dx.doi.org/10.2138/am-2017-6125

Table 2. Representative electron microprobe analysis of the ore minerals from the Moutoulas mineralization, Serifos.

Mineral	Pyrite (1)	Sphalerite (2)	Sphalerite (3)	Tetrahedrite-tennantite (4)	Tennantite-Tetrahedrite (5)	Galena (6)	Hessite (7)	Melonite (8)	Tetradymite (9)	Bismuthinite (10)	Native Bi (11)	Bismite (12)	Bismutite (13)	Beyerite (14)
Elements wt.%	N=17	N=6	N=7			N=25	N=4		N=1	N=10	N=12	N=5	N=7	N=4
Ag				0.42	0.39		62.80		0.83		0.41			
Cu				40.52	40.56		0.48	0.28	0.32					
Zn		50.60	58.37	5.38	5.36									
Pb				0.19	0.20	85.04		0.31						1.34
Fe	46.54	14.99	7.98	0.15	0.09									
Ni								18.63						
Bi	0.24			3.31	4.05	1.12			58.69	80.53	99.52	89.39	81.24	67.51
Te				2.01	2.07	0.02	36.66	80.35	35.95	0.26	0.02			
As	0.38			8.46	10.34	0.02								
Sb				13.02	10.89	0.03								
Se						0.01								
Ca														7.36
O												10.29	15.00	20.19
C													2.55	3.35
S	52.82	33.50	33.26	26.44	25.89	12.89	0.55	0.04	4.46	18.57	0.03			
Total	99.89	99.09	99.61	99.90	99.84	99.96	100.48	99.61	100.25	99.36	99.97	99.68	97.99	99.74
Ag							1.99[i]		0.05[m]		0.01[q]			
Cu				10.40[d]	10.40[d]		0.01[i]	0.02[k]	0.03[m]					
Zn		0.74[c]	0.71[c]	1.60[d]	1.60[d]									
Pb						1.00[g]								0.04[r]
Fe	1.00[a]	0.26[c]	0.29[c]											
Ni								0.98[k]						
Bi	0.01[b]			0.31[e]	0.31[e]	0.01[h]			1.92[m]	2.00[o]	0.99[q]	2.00	1.99	2.00
Te				0.30[f]	0.30[f]		0.98[j]	2.00[l]	2.03[n]	0.02[p]				
As	0.01[b]			2.00[e]	2.40[e]									
Sb				2.00[e]	1.60[e]									
Se														
Ca														0.96[r]
O												3.00[p]	5.00[q]	8.00
C													1.13	
S	1.98[b]	1.00	1.00	12.40[f]	12.40[f]	0.99[h]	0.02[j]		1.00[n]	2.98[p]				

(1). [a]Fe=1, [b]S+Bi+As=2, Zn+Cu/Zn+Cu+Fe=35.7 and As/As+S = 0.67
(2). and (3). [c]Zn+Fe = 1, $X_{FeS\%}$ = 25.8 (stage I) and $X_{FeS\%}$ = 13.8 (stage II)
(4). and (5). [d]Cu+Zn = 12, [e]As+Sb+Bi=4, [f]S+Te=13, As/As+Sb+Bi=0.48, Bi/As+Sb+Bi=0.04 with formula: $Cu_{10.4}Zn_{1.6}(As_{1.9}Sb_{1.9}Bi_{0.2})S_{12.4}Te_{0.6}$ and As/As+Sb+Bi=0.58, Bi/Te+Bi+S=0.04, with formula: $Cu_{10.4}Zn_{1.6}(As_{1.9}Sb_{1.9}Bi_{0.2})S_{12.4}Te_{0.6}$
(6). [g]Pb=1, [h]S+Bi=1
(7). [i]Ag+Cu=2, [j]Te+S=1, Te/Te+S = 0.99, Cu/Ag+Cu = 0.18, Ag_2Te, $Ag_{1.9}Cu_{0.1}Te_{0.99}S_{0.1}$
(8). [k]Ni+Cu=1,[l]Te=2.0
(9). [m]Bi+Au+Cu=2,[n]S=1, Te=2, S/Te+S =0.33
(10). [o]Bi=2,[p]S+Te=3,
(11). [q]Bi+Ag=1,
(12). [p]Based on 3 oxygens.
(13). [q]Based on 5 oxygens, Bi=2
(14). [r]Based on 8 oxygens, Bi=2.

Always consult and cite the final, published document. See http:/www.minsocam.org or GeoscienceWorld

This is a preprint, the final version is subject to change, of the American Mineralogist (MSA)
Cite as Authors (Year) Title. American Mineralogist, in press.
(DOI will not work until issue is live.) DOI: http://dx.doi.org/10.2138/am-2017-6125

Table 3. Primary L-V fluid inclusion microthermometric data for individual fluid inclusion assemblages.

Sample	Mineral	Size (μm x μm)	V/V+L (%)	$T_{f\text{-}ice}$ (˚C)	$T_{m\text{-}ice}$ (˚C)	T_h (˚C)	wt.% NaCl equivalent
SE1	Clear quartz (stage I)	8.0 to 5.5	5 to 13	-22.7 to -21.7	-3.7 to -2.4	229 to 251	4.0 to 5.3
SE1	Sphalerite (stage I)	5.0 to 6.5	8 to 10	-22.7 to -21.3	-3.6 to -2.8	239 to 245	4.8 to 5.7
SE1	Clear quartz (stage II)	6.5 to 4.5	11 to 13	-23.2 to -21.5	-2.1 to -3.4	220 to 227	3.4 to 5.4
SE1	Sphalerite (stage II)	5.5 to 7.5	2 to 6	-23.8 to -21.5	-2.3 to -2.2	218 to 226	3.7 to 3.9
SE2	Clear quartz (stage III)	9.0 to 5.0	8 to 16	-23.8 to -21.1	-3.3 to -2.4	203 to 214	3.4 to 4.8
SE2	Clear quartz (stage IV)	6.0 to 6.5	8 to 14	-23.8 to -21.8	-3.4 to -2.3	190 to 197	1.3 to 4.9

Always consult and cite the final, published document. See http:/www.minsocam.org or GeoscienceWorld

This is a preprint, the final version is subject to change, of the American Mineralogist (MSA)
Cite as Authors (Year) Title. American Mineralogist, in press.
(DOI will not work until issue is live.) DOI: http://dx.doi.org/10.2138/am-2017-6125

Table 4. Compositions of primary L-V fluid inclusions based on Raman spectroscopic data.

Sample	Mineral	X_{H2O} (mol%)	X_{CO2} (mol%[A,B])	X_{H2S} (mol%)	X_{O2} (mol%)	X_{H2} (mol%)	$\log(X_{CO2/H2O})$	$\log(X_{O2/H2O})$	$\log(X_{H2S/H2O})$	T (°C)
SE1	Clear quartz (stage I)	84.0 to 85.1	12.2 to 14.0	1.2 to 1.7	0.0 to 0.1	0.5 to 0.9	-0.8 to -0.7	-3.4 to -3.2	-1.8 to -1.7	235 to 248[A,B]
SE2	Clear quartz (stage IV)	84.5 to 90.1	8.7 to 14.6	0.0 to 0.1	0.0 to 0.1	0.7 to 0.9	-1.0 to -0.8	-3.0 to -2.8	-3.5 to -2.9	190 to 197[A,B]

Temperature estimates were based on geothermometers [A]CO_2- of Arnórsson & Gunnlaugsson (1985), [B]CO_2/H_2S- of Nehring & D'Amore (1984).

Always consult and cite the final, published document. See http:/www.minsocam.org or GeoscienceWorld

This is a preprint, the final version is subject to change, of the American Mineralogist (MSA)
Cite as Authors (Year) Title. American Mineralogist, in press.
(DOI will not work until issue is live.) DOI: http://dx.doi.org/10.2138/am-2017-6125

Table 5. Compositions of primary L-V fluid inclusions based on bulk composition chromatographic data.

Sample	Si^{4+} (ppm)	Na^{+} (ppm)	K^{+} (ppm)	Mg^{2+} (ppm)	Ca^{2+} (ppm)	Cl^{-} (ppm)	SO_4^{2-} (ppm)	HCO_3^{-} (ppm)
SE1	314.1 to 354.9	3.7 to 3.9	1.6 to 1.7	10.8 to 11.0	20.8 to 21.2	18.9 to 19.7	20.2 to 19.6	28.7 to 30.1
SE2	18.4 to 19.6	2.2 to 2.3	0.8 to 0.9	1.6 to 1.9	7.46 to 7.92	3.4 to 4.1	8.3 to 9.6	16.5 to 17.2

T (°C)	$\log(Si^{4+}/Na^{1+}+K^{1+}+Mg^{2+}+Ca^{2+})$	$\log(Cl^{1-}/SO4^{2-})$	$\log(Cl^{1-}/HCO_3^{1-})$	$\log(\Sigma cations/\Sigma anions)$
240 to 242[A]	2.1	0.0	-0.2	2
191to 195[A]	1.3	-0.4 to -0.3	-0.7 to -0.6	1.6

Temperature estimates were based on the Na-K-Ca geothermometer of Fournier and Truesdell (1973). For the Na-K-Ca geothermometer the log $\sqrt{Ca/Na} + 2.06$ values are positive and T ≥ 100°C and so $\beta = 3/4$.

Always consult and cite the final, published document. See http:/www.minsocam.org or GeoscienceWorld

This is a preprint, the final version is subject to change, of the American Mineralogist (MSA)
Cite as Authors (Year) Title. American Mineralogist, in press.
(DOI will not work until issue is live.) DOI: http://dx.doi.org/10.2138/am-2017-6125

Table 6. Sulfur and lead isotope data for pyrite, sphalerite, chalcopyrite, greenockite and galena from the Moutoulas vein system, Serifos.

Sample	Mineral	$\delta^{34}S$	T[1] (°C)	$\delta^{34}S_{H2S}$[2]	$^{206}Pb/^{204}Pb$	$^{207}Pb/^{204}Pb$
SE1	Pyrite (stage I)[A]	4.83	249	2.28	18.863	15.653
SE2	Pyrite (stage I)[A]	3.78	249	3.33	18.867	15.657
SE3	Pyrite (stage I)	4.44	249	2.94	18.871	15.661
SE4	Pyrite (stage I)	4.12	249	2.62	18.868	15.659
SE1	Sphalerite (stage I)[A]	3.73	249	3.33	-	-
SE2	Sphalerite (stage I)[A]	2.69	249	2.29	-	-
SE3	Sphalerite (stage II)[B]	3.54	226	3.14	-	-
SE2	Chalcopyrite (stage I)	5.08	249	4.88	-	-
SE3	Greenockite (stage II)[B]	5.49	226	4.79	-	-
SE1	Galena (stage III)	5.62	200	3.02	18.896	15.687
SE2	Galena (stage III)	5.04	200	2.44	18.902	15.694
SE3	Galena (stage III)	5.37	200	2.77	18.892	15.702

[1]Temperatures obtained from fluid inclusion data, the CO_2-, CO_2/H_2S-, and Na-K-Ca geothermometers (Tables 3 and 4) and the [A]pyrite-sphalerite and [B]sphalerite-greenockite pairs; according to the equations of Ohmoto and Rye (1979), Ohmoto and Lasaga (1982) and Li and Liu (2006).

[2]Utilizing the H_2S-sulfide equations of Ohmoto and Rye (1979), Ohmoto and Lasaga (1982) and Li and Liu (2006).

Always consult and cite the final, published document. See http:/www.minsocam.org or GeoscienceWorld

Table 7. Reactions and corresponding values of selected physicochemical parameters applicable to the mineralizing fluid at Moutoulas, for temperatures of 250º, 200º and 25ºC and an ionic strength I = 0.20.

	Reaction	T (°C)	Calculated physicochemical parameters
1	$3KAlSi_3O_{8(s)} + 2H^+_{(aq)} = KAl_3Si_3O_{10}(OH)_{2(s)} + 6SiO_{2(aq)} + 2K^+_{(aq)}$	250[A]	$\log(\alpha_{K^+}/\alpha_{H^+}) = 3.7$, pH = 5.4
2	$3NaAlSi_3O_{8(s)} + 2H^+_{(aq)} + K^+_{(aq)} = KAl_3Si_3O_{10}(OH)_{2(s)} + 6SiO_{2(aq)} + 3Na^+_{(aq)}$	250[A]	$\log(\alpha_{Na^+}/\alpha_{H^+}) = 2.4$, pH = 5.4
3	$NaAlSi_3O_{8(s)} + K^+_{(aq)} = KAlSi_3O_{8(s)} + Na^+_{(aq)}$	250[A]	$\log(\alpha_{K^+}/\alpha_{Na^+}) = 0{,}73$, pH = 5.4
4	$2FeS_{2(s)} = 2FeS_{(s)} + S_{2(g)}$	250[A]	$\log fS_{2(g)} = -13.8$
5	$2H_2O_{(g)} = O_{2(g)} + 2H_{2(g)}$	250[A], 200[B]	$\log fO_{2(g)} = -39.2$ and -43.5
6	$Bi_2S_{3(s)} = 2Bi_{(s)} + 1.5S_{2(g)}$	200[B]	pH = 6.5
7	$2Bi_2S_{3(s)} + 6H_2O_{(l)} = 4Bi_{(s)} + 6H^+_{(aq)} + 6HS^-_{(aq)} + 6O_{2(g)}$	200[B]	$\log fS_{2(g)} = -16.5$
8	$H_2S_{(aq)} = H^+_{(aq)} + HS^-_{(aq)}$	250, 200[B]	$\log\alpha_{HS^-_{(aq)}} = -1.8$ and -2.9
9	$2H_2S_{(aq)} + O_{2(g)} = S_{2(g)} + 2H_2O_{(l)}$	250, 200[B]	$\log\alpha_{HS^-_{(aq)}} = -1.8$ and -2.9
10	$Ag_2Te_{(s)} + H_2O_{(l)} = 2Ag_{(s)} + H_2Te_{2(aq)} + 0.5O_{2(g)}$	200[B]	$\log\alpha_{H2Te(aq)} = -5.2$
11	$2H_2Te_{(aq)} + O_{2(g)} = Te_{2(g)} + 2H_2O_{(l)}$	200[B]	$\log fTe_{2(g)} = -17.0$
12	$H_2Te_{(aq)} = H^+_{(aq)} + HTe^-_{(aq)}$	200[B]	$\log\alpha_{HTe^-_{(aq)}} = -3.8$
13	$2Bi(OH)_2^+_{(aq)} + 2H_2Te_{(aq)} + H_2S_{(aq)} = Bi_2Te_2S_{(s)} + 4H_2O_{(l)} + 2H^+_{(aq)}$	200[B]	$\log\alpha_{H2S(aq)} = -3.7$
14	$2Bi_{(s)} + 1.5O_{2(g)} + 4H^+_{(aq)} = 2Bi(OH)_2^+_{(aq)} + H_2O_{(l)}$	250[A], 200[B], 25	$\log\alpha Bi(OH)^{+2}_{(aq)} = -14.0, -11.2, -10.3$. pH = 7.1
15	$4Bi(OH)_2^+_{(aq)} + HCO_3^-_{(aq)} + O_{2(g)} + H_2O_{2(l)} = (BiO_2)_2CO_{3(s)} + Bi_2O_{3(s)}$	25	$\log fO_{2(g)} = -32.5$

[A]250° and [B]200°C, temperatures based on fluid inclusions, the CO_2-, CO_2/H_2S- and Na-K-Ca-geothermometers, and pyrite-sphalerite and sphalerite-greenockite isotopic pairs (Tables 3, 4 and 5).
The thermodynamic properties of bismuth complexes were compiled from Skirrow and Walshe (2002); Tooth et al. (2008, 2011); Staude et al. (2012) and Zhou et al. (2016).
For reactions 5, 11, 12, 13, 14 and 15 the logK values are -5.2, -4.7, -1.1, +11.7, +6.9 and -12.6, respectively.

This is a preprint, the final version is subject to change, of the American Mineralogist (MSA)
Cite as Authors (Year) Title. American Mineralogist, in press.
(DOI will not work until issue is live.) DOI: http://dx.doi.org/10.2138/am-2017-6125

Supplementary data

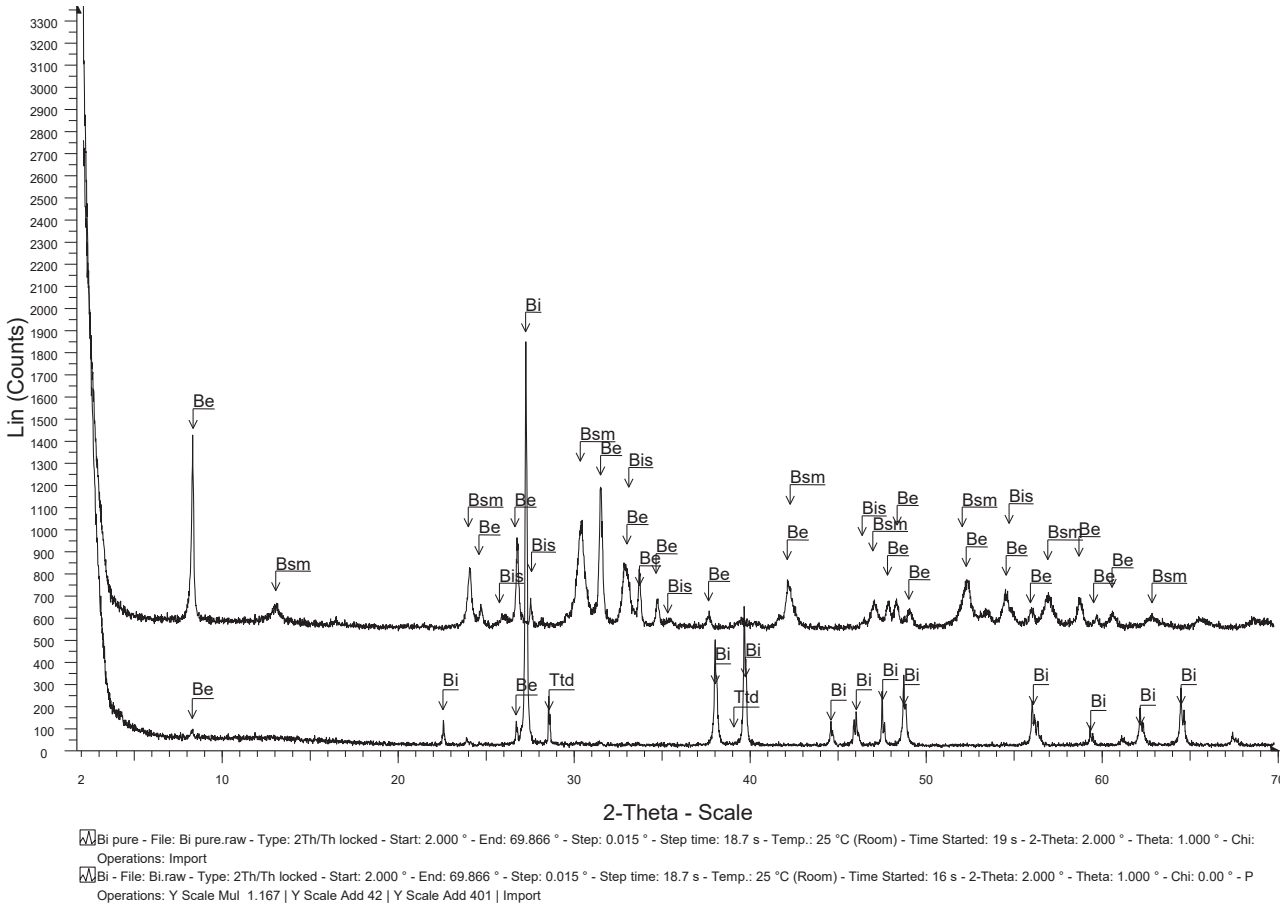

Always consult and cite the final, published document. See http:/www.minsocam.org or GeoscienceWorld